Opto-Electronic Advances

Original Article

2023, Vol. 6, No. X

DOI: 10.29026/oea.2023.220061

Janus aramid nanofiber aerogel incorporating plasmonic nanoparticles for high-efficiency interfacial solar steam generation

Hui Zhang[1,2†], Lei Feng[1,2†], Fengyue Wang[1], Mingze Liu[1], Yingying Zhang[1], Jia Zhu[1,2], Yanqing Lu[1,2] and Ting Xu[1,2*]

Interfacial solar steam generation (ISSG) is a novel and potential solution to global freshwater crisis. Here, based on a facile sol-gel fabrication process, we demonstrate a highly scalable Janus aramid nanofiber aerogel (JANA) as a high-efficiency ISSG device. JANA performs near-perfect broadband optical absorption, rapid photothermal conversion and effective water transportation. Owning to these features, efficient desalination of salty water and purification of municipal sewage are successfully demonstrated using JANA. In addition, benefiting from the mechanical property and chemical stability of constituent aramid nanofibers, JANA not only possess outstanding flexibility and fire-resistance properties, but its solar steaming efficiency is also free from the influences of elastic deformations and fire treatments. We envision JANA provides a promising platform for mass-production of high-efficiency ISSG devices with supplementary capabilities of convenient transportation and long-term storage, which could further promote the realistic applications of ISSG technology.

Keywords: plasmonics; interfacial solar steam generation; broadband optical absorption; aerogel

Zhang H, Feng L, Wang FY, Liu MZ, Zhang YY et al. Janus aramid nanofiber aerogel incorporating plasmonic nanoparticles for high-efficiency interfacial solar steam generation. *Opto-Electron Adv* **6**, 220061 (2023).

Introduction

Global demands for freshwater are steadily increasing to meet the growth of human population, development of industrial manufacture and expansion of agricultural irrigation[1,2]. Traditional water production techniques, such as reverse osmosis[2,3] and multi-stage flash[4], rely on costly infrastructures and high consumption of electric or fossil energy. Innovation of low-cost, energy-efficient and eco-friendly water desalination and purification devices has now been a key issue for future human lives. Solar-induced distillation is one candidate to relieve the water and energy crisis, which uses solar-thermal energy to extract freshwater from sea or waste water[5–7]. However, due to the low optical absorption and high thermal capacity of water, direct solar-thermal distill of bulk water is lacking in efficiency. To evaporate bulk water, a large amount of energy is required, which is insufficiently supplied by the photothermal absorption of water itself and easy to be wasted into the environment. Alternatively, interfacial solar steam generation (ISSG) is of high energy utilization[8–10]. An ideal ISSG device is usually a 2D film or a 3D block floating on water which typically consists

[1]National Laboratory of Solid-State Microstructures, Jiangsu Key Laboratory of Artificial Functional Materials, College of Engineering and Applied Sciences, Nanjing University, Nanjing 210093, China; [2]Collaborative Innovation Center of Advanced Microstructures, Nanjing 210093, China.
[†]These authors contributed equally to this work.
*Correspondence: T Xu, Email: xuting@nju.edu.cn

Received: 1 April 2022; Accepted: 18 July 2022 ; Published online: 23 November 2022

of an optical absorber on the top and a water transporter at the bottom. The absorber should perform intensive and omnidirectional absorption with a broad operation band covering the solar spectrum for the maximum utilization of solar energy. The transporter should be porous, hydrophilic and adiabatic. The porous structure can divide bulky water into micro/nano scale branches and the hydrophilicity-induced capillary forces drive the water branches approaching to the light absorber for efficient water transportation. The adiabaticity hinders heat conduction from the absorber to the bulky water, and thus reduces the energy waste. Consequently, direct energy transfer from the light absorber to the water branches facilitates the high-efficiency generation of solar steam[11].

Increasing the area of steam generators leads to a higher total output of freshwater during the practical desalination or purification processes. The area scale mainly depends on the constituent materials and the fabrication regimes. For example, the self-assembled plasmonic nanoparticle membrane is an early proof-of-concept ISSG device[12]. However, it is mechanically vulnerable and impossible to be scaled up due to the discrete configuration. Template-assisted techniques, such as assembly of nanoparticles[13,14], deposition of metal[15], or electro-polymerization of conductive macromolecules[16,17], can realize production of steam generators with higher mechanical strength. Nevertheless, the generators' scales are limited by the lithographic templates which usually reach no more than several square centimeters. Instead, carbon materials[18–24], biomass derivatives[25–27], cellulose-based composites[28–30], electrospun nanofibers[31], hydrogels[32–36], and aerogels[37–41] suit better for scalable ISSG device production which are robust and template-free. Among them, aerogel is one kind of novel materials with great porosity and adiabaticity. It is a 3D cross-linked network of micro/nano components with plentiful pores where a large amount of air is trapped. As a result, aerogel is not only lightweight because the highly loaded air can greatly lower the gel density, but also soft and flexible. These advantages further benefit the transport of large-scale devices, which can be easily shaped such as cut, stretched, bent or curled. However, aerogel-based ISSG devices are usually either limited in evaporation efficiency[37–39], or forced to be incorporated with auxiliary equipment (e.g. solar cells[38] or compound parabolic concentrators[41]) to achieve high-efficiency steam generation, which leads to high complexity of the purification configurations.

Besides the transport, for the safety of storage, an ISSG device should be chemically stable to avoid potential risks of fire danger. Due to the optical absorptivity and thermal adiabaticity, mass-stored large-scale ISSG devices can easily trap a large amount of light energy, which may result in severe increment of temperature. In this case, some ISSG devices based on celluloses, carbon materials, or flammable polymers are unfavorable. To our knowledge, flammability is usually neglected in previous researches and only few literatures highlighted combustion tests[42,43]. Accordingly, developing a scalable, flexible, and fireproof aerogel as a high-efficiency steam generator has become challenging and crucial for wide generalization and practical application of ISSG technology.

Herein, we present a Janus aramid nanofiber aerogel (JANA) as an interfacial solar steam generator. JANA is fabricated based on the commercial Kevlar threads, which is a commonly used flexible and refractory material at macroscale[44,45], and Au nanoparticle using a facile and scalable sol-gel technique. It is of a bilayer configuration incorporating an intensive, omnidirectional and broadband optical absorber and a porous, adiabatic, hydrophilic water transporter. Using JANA, high-efficiency solar steam generation, desalination of salty water and purification of municipal sewage are successfully demonstrated. Moreover, JANA features high mechanical strength and chemical stability, respectively resulting in excellent flexibility and fire resistance. These advantages make JANA facilitate the ISSG devices in industrial manufacture, transport and storage.

Results and discussions

Scalable fabrication and characterization of Janus aramid nanofiber aerogel (JANA)

Figure 1 illustrates the sol-gel process-based fabrication procedure of JANA. Commercial Kevlar threads (Fig. 1(a)) are firstly dispersed in dimethyl formamide and forming a yellow suspension of aramid microfibers (Fig. 1(b)). Dimethyl formamide can swell and loosen the Kevlar threads. Afterwards, aramid microfibers are treated with a mixed solution of dimethyl sulfoxide and potassium hydroxide to disassemble microfibers forming a dark-red and viscous sol of aramid nanofibers (Fig. 1(c)). This disassembly is caused by the deprotonation of amide groups[46]. The sol is then added with phosphoric

Fig. 1 | The fabrication process of JANA for interfacial steam generation. (**a**) Photograph of commercial Kevlar threads. (**b**, **c**) Photograph and schematic illustration of aramid microfiber suspension and aramid nanofiber sol, respectively. (**d**) Photograph of aramid gel, whose top surface is sprayed with Au nanoparticle suspension. (**e**) Photograph of JANA and schematic illustrations depicting the microscopic morphology of the upside PANA and the downside ANA, respectively. (**f**) Schematic illustration of the steam generation process using JANA.

acid and glutaraldehyde. During stirring and settling, phosphoric acid can catalyze the hydrolysis of the aramid nanofibers generating reactive NH_2 and COOH function groups, which can bond to glutaraldehyde and form cross-linked 3D network structures, i.e. aramid gel. The gel is then extracted by filtration and washed using dimethyl sulfoxide to remove residual solutes. Next, the top surface of the gel is uniformly sprayed with Au nanoparticle suspension (Fig. 1(d)), which is synthesized using a typical citrate reduction method[47]. The aramid nanofibers and Au nanoparticles are mutually combined based on the hydrogen bondings between the amide groups of aramid and the carboxylic acid groups of the citrates coated on Au nanoparticles. The chemical process is verified by Fourier transform infrared (FT-IR) spectroscopy results (Fig. S1 of Supplementary information (SI)). The Au-gel composite is finally freeze-dried to remove the inside water forming the JANA (Fig. 1(e)). The aramid nanofiber network contains plentiful micro/nano pores. The sprayed Au nanoparticle suspension can only penetrate to a certain depth by carefully controlling the suspension volume. As a result, JANA is of a bilayer configuration. As depicted in Fig. 1(e), the black upside is a plasmonic aramid nanofiber aerogel (PANA), i.e. the composite consisting of an aramid nanofiber network and Au nanoparticles; the yellow downside is an aramid nanofiber aerogel (ANA), i.e. an aramid nanofiber network without Au nanoparticles. Figure 1(f) conceptually illustrates that JANA can float on water and serve as an effective steam generator resulted from the synergistic contributions of PANA and ANA. The downside ANA contains plentiful channels to divide bulky water into branches, which are guided approaching to the Au nanoparticles embedded in the upside PANA. Au nanoparticles can concentrate light by plasmonic resonances and realize the photothermal energy conversion. Direct heat transfer from the light concentrators to the water branches leads to high-efficiency local interfacial evaporation. Finally, the generated steam escapes from JANA surface through the pores spread all over the nanofiber aerogel.

Since each procedure in the sol-gel process is chemically engineered and free from lithographic technique, the production of JANA is highly scalable. As shown in Fig. 2(a), we fabricate a large-scale JANA sample with the size of 60 cm × 45 cm as an instance to demonstrate its scalability. For investigation of the microscopic morphology of JANA, bottom ANA and upside PANA are respectively characterized using scanning electron microscopy (SEM). As shown in Fig. 2(b), ANA is a 3D network comprising of aramid nanofibers, whose profiles are well-defined. The average fiber diameter is about 54

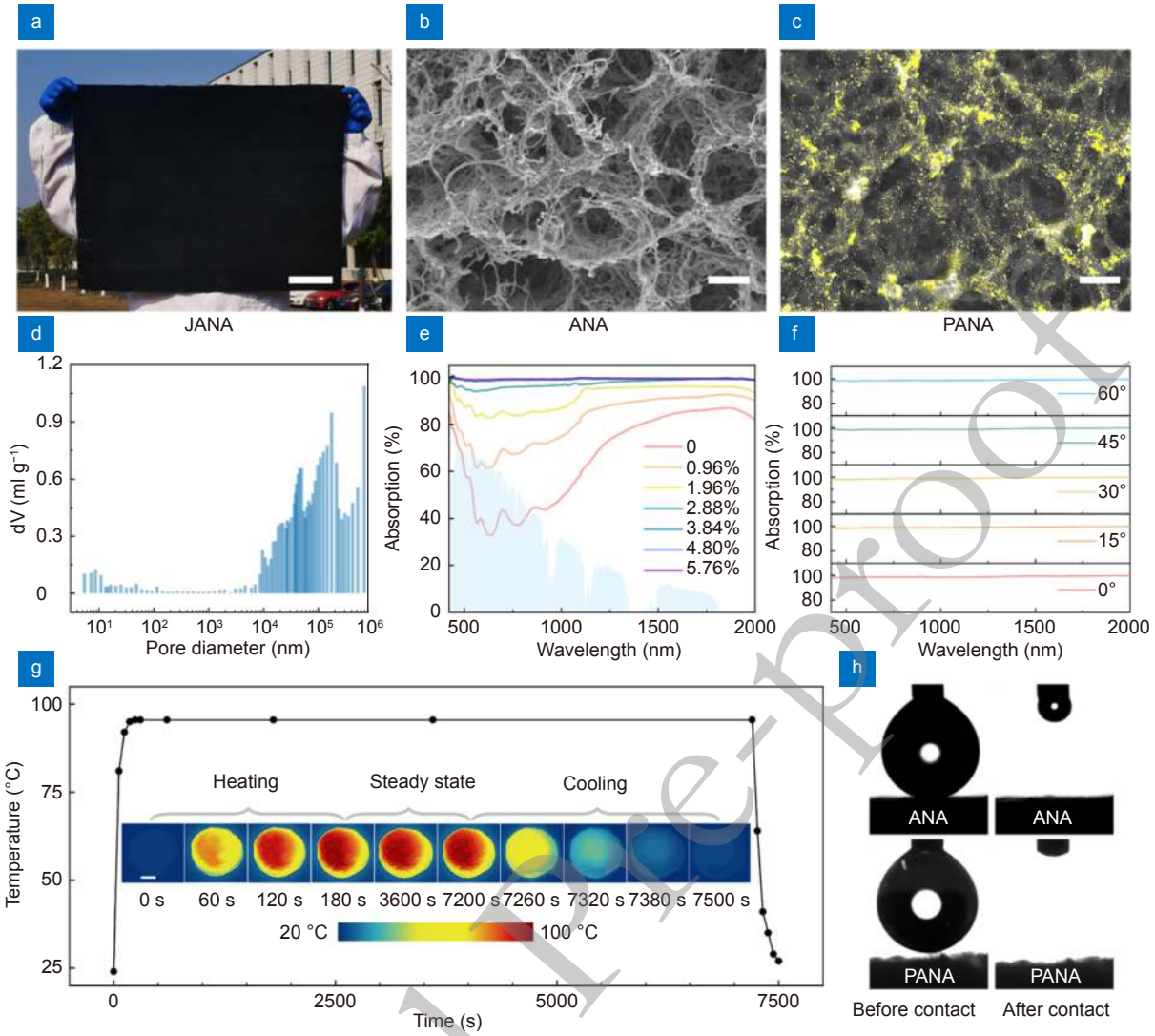

Fig. 2 | Characterizations for morphology, optical absorption, photothermal responses and wettability. (**a**) Photograph of a large-area JANA cloth with the size of 60 cm × 45 cm. The scale bar stands for 10 cm. (**b**) SEM images of ANA. The scale bar stands for 1 μm. (**c**) SEM images of PANA, in which Au nanoparticles are highlighted using yellow fake color. The scale bar stands for 1 μm. (**d**) Correlation between the differential pore volume and the pore diameter in 1 gram of JANA measured using mercury intrusion method. (**e**) Absorption spectra of JANA samples with different weight fractions of Au nanoparticles. The blue area represents normalized power of solar irradiating power. (**f**) Absorption spectra of JANA under sources with different incident angles. (**g**) Correlation between the temperature variation of JANA and time using switched illumination by a solar simulator with 1-sun output power. Insets are IR images of the JANA at different moments during the photothermal test. (**h**) Photographs of an ANA and a PANA approaching to a water droplet, respectively.

nm and the length can reach a few microns, resulting in high aspect ratios. The slender nanofibers mutually interlace and form the porous network. As shown in Fig. 2(c), PANA is ANA decorated with Au nanoparticles, which are highlighted using fake yellow color. The average diameter of Au nanoparticles is about 43 nm. In PANA, the profiles of the nanofibers are blurred. Adjacent nanofibers draw close to each other forming thicker skeletons of the aramid network and thus smaller pores. This is due to an adhesive effect caused by the sedimentation of the residual solutes in the Au nanoparticle suspension. We further use mercury intrusion method to statistically characterize the porous morphology of JANA. A portion of the pores are open-ended and can be filled with mercury under high pressure. The other pores are enclosed and inaccessible to mercury. In this case, the acquired porosity equals to 91%. Namely, more than 91% volume of JANA is filled with air, resulting in its lightweight feature and the density of JANA is only 0.0214 g cm^{-3}. Figure 2(d) shows the correlation between the differential pore volume and diameter in one gram of JANA. Large pores, whose diameter ranging from tens to

a few hundred microns, occupy the major volume within the total pore space. Compared with small ones, they perform lower resistance of mass transfer, facilitating the flow of water branches and the escape of solar steam.

The optical absorption of JANA is optimized by adjusting the content of the loaded Au nanoparticles. Since all the Au nanoparticle suspension can be fully reserved in JANA, it is easy to precisely control the loading capacity of Au nanoparticles by spraying specific volumes of the suspension. In this case, seven pieces of JANA with different Au weight fractions ranging from 0 to 5.76% (Fig. S2 of SI) are fabricated and characterized using an absorption spectrograph, as shown in Fig. 2(e). The light source is unpolarized and the spectrum ranges from 400 nm to 2000 nm, which covers the main solar band as denoted by the blue area in Fig. 2(e). With no Au nanoparticle loaded, JANA performs limited optical absorption, whose average absorbance is about 66.7%. With the increment of Au content, the absorbance gradually increases over the entire band. When the Au content is 3.84%, the average absorbance surpasses 99%. Continued increments of the Au content make nearly no influence to the optical absorption. For balancing the tradeoff between low fabrication cost and high optical absorption, we choose the JANA with 3.84 wt% Au as the optimized sample for the following experiments. The angle dependence is also investigated, as shown in Fig. 2(f). By varying the incident angles from 0° to 60°, the profiles of the absorption spectra are nearly the same with a constant average absorbance higher than 99%. The excellent absorption performances can be attributed to a comprehensive optical mechanism combining i) anti-reflection effect, ii) localized surface plasmon resonance (LSPR) and iii) non-resonant decay. Anti-reflection is the premise for high absorption insuring that sufficient optical energy can passes through the air-JANA interface rather than being reflected. It is generated from the low difference of refractive indices between air and JANA. Due to the highly porous morphology, the textured JANA surface can trap plentiful air bubbles lowering the effective refractive index and vanishing any interface where the refractive index changes abruptly. Because of the diversity of the pore size and orientations, this anti-reflection effect is independent to incident wavelengths and angles[11]. In this case, light energy can enter JANA and be dissipated into heat via LSPR of Au nanoparticles and non-resonant decay of aramid nanofibers[48]. For the former, LSPR generates intensive optical extinction. The resonant wavelength of LSPR is dependent to the size of Au nanoparticles. Monodispersed Au nanoparticles tend to perform narrowband absorption and scattering at one single specific wavelength within the visible band. However, aggregates of Au nanoparticles can be also formed in a variety of shapes and sizes, which makes the resonant wavelengths red-shifted in varying degrees. Broadband light can be directly absorbed by surface plasmon of Au nanoparticles, or scattered leading to the change of propagation directions and the extend of light paths. For the latter, non-resonant decay generates weak optical absorption. It is caused by the intrinsic extinction of aramid nanofibers. Nevertheless, the non-resonant absorption efficiency can be improved to increase the light-aramid interaction by lengthening the light paths in JANA resulted from the LSPR scattering and the increment of JANA thickness[45]. The absorption mechanism is numerically investigated and verified by using finite-difference time-domain simulations (Fig. S3 of SI). Resultingly, JANA can be qualified as a near-perfect broadband optical absorber.

Next, the photothermal property of JANA is explored. Based on energy conservation law, since all the optical energy is transformed into heat without any other form of energy, a good light absorber is equivalent to a good heater. Thus, JANA can serve as an efficient light-heater, which is characterized by monitoring the real-time temperature using an IR thermal-imaging camera under switched illumination of a solar simulator, as shown in Fig. 2(g). The solar simulator output is equal to 1 time of sun power. The ambient temperature is about 22 °C. The temperature of JANA is calculated by averaging the temperature values of all the pixels at the top surface of the JANA sample captured in the IR images. Without the illumination of solar simulator, the temperature of JANA is 24 °C. The 2 °C difference is caused by the absorption of ambient light. Switching on the solar simulator, the temperature dramatically increases to 96 °C within 180 s and reaches a steady state. At the time of 7200 s, the illumination is switched off and the temperature decreases to 26 °C within 300 s. This process exhibits the features of fast heating and relatively slow cooling. IR images (insets in Fig. 2(g)) show the temperature distribution of the JANA surface at different moments. The flare area is slightly smaller than JANA. After switching on the source, temperatures in the center (illuminated area) are higher than those on the edge (unilluminated area), featuring evident heat generation and confinement. The

photothermal responses are not only resulted from near-perfect optical absorption, but also the low heat conductivity of JANA (0.061 W m^{-1} K^{-1}, at 25 °C, which is due to the high porosity and the low heat conductivity of air). Near-perfect optical absorption guarantees that light energy is efficiently absorbed in JANA and transformed into heat. Meanwhile, low heat conductivity retards the energy dissipation to the environment. Consequently, JANA is able to achieve high-efficiency photothermal conversion.

The wettability of JANA is characterized using a drop shape analyzer. ANA and PANA are respectively tested, as shown in Fig. 2(h). Both of them feature a super-hydrophilic surface, on which the droplet spread out extremely fast right after the droplet-surface contact. The dropping processes take too little time to catch the contact moments as shown in Supplementary video S1. The super-hydrophilicity originates from both the chemical hydrophilicity of aramid and the high surface roughness. The chemical hydrophilicity is proved by measuring the contact angle of a dense aramid film, which equals to 47°, as shown in Fig. S4 of SI. On the other side, the high surface roughness is generated from the porous configurations of ANA and PANA. Moreover, the hydrophilic nanofiber networks can impale the droplet and divide it into small branches, which flow into the open-ended pores driven by the capillary forces. As a result, JANA is highly wettable and provides plentiful channels for effective water delivering. Although the weight of JANA is increased after wetting, wet JANA can still float on water. This is attributed to the enclosed pores which cannot be penetrated by water and maintain a low aerogel density.

JANA for solar steam generation

Since JANA contains an efficient light-heater in the top (PANA) and an effective water-transporter in the bottom (ANA), it meets the regime of an ideal ISSG device. Therefore, we systematically investigate its solar steaming performances. As shown in Fig. 3(a), we build a photo-thermo-gravimetry, where a piece of JANA sample floats in a beaker of water. A solar simulator is used with 1-sun output power to heat up the JANA sample. Real-time temperatures are recorded using two IR cameras simultaneously from the top and side views. The mass change of water is recorded using an electronic balance. Figure 3(b) and 3(c) are the captured top- and side-view IR images of the beakers with and without JANA floating in water, respectively. With time, heat is continuously delivered from the top to the bottom of the beakers and water are gradually warmed up to steady states. The steady temperatures of the JANA-air interface and the water-air interface are about 51 °C and 31 °C, respectively, which are calculated by averaging the temperature values of all the pixels at the two interfaces shown in the IR images. For the beaker with JANA, water near to the interface is much hotter than that underneath, implying that JANA can highly absorb and locally concentrates the photothermal energy. Referring to the temperature of JANA in air under the same light source with equal output power, which reaches 96 °C, the temperature of JANA in water is 45 °C lower. This decrement can be mainly attributed to the heat transfer to the delivered water inside the nanofiber porous network for enhancing the interfacial steam generation. By contrast, for the case without JANA (Fig. 3(c)), the thermal distribution inside the beaker is rather uniform, indicating the entire bulk of water has nearly the same low temperature, which significantly reduces the steam generation efficiency.

Next, we quantificationally investigate the water evaporation efficiency, which is characterized by recording the mass decrement of water normalized to the case per square meter of JANA, as shown in Fig. 3(d). Under 1-sun illumination by the solar simulator for 12 h, the mass decrement of water with and without JANA are respectively 28.43 kg m^{-2} and 4.67 kg m^{-2}. In other words, JANA can significantly enhance the evaporation rate from 0.39 kg m^{-2} h^{-1} to 2.37 kg m^{-2} h^{-1}. We further calculate the evaporation rate during each hour, as shown in Fig. 3(e). At first, the evaporation rates with and without JANA both tend to gradually increase. After about 2 h, the evaporation rates are nearly constant, featuring a quasi-steady state of steam generation. The slight fluctuation is due to the variations of ambient temperature and airflow. The highest evaporation rate with JANA is about 2.68 kg m^{-2} h^{-1}, which is higher than the average level for previously reported ISSG devices. This benefits from the comprehensive contributions of JANA, including near-perfect optical absorption, efficient photothermal concentration, porous morphology and chemical hydrophilicity. Especially, the plentiful pores in the aramid aerogel can facilitate water to be divided into small clusters lowering the evaporation enthalpy[49].

Besides evaporation rate, another important factor to evaluate an ISSG device is the reusability under salty condition in the desalination application. The interfacial

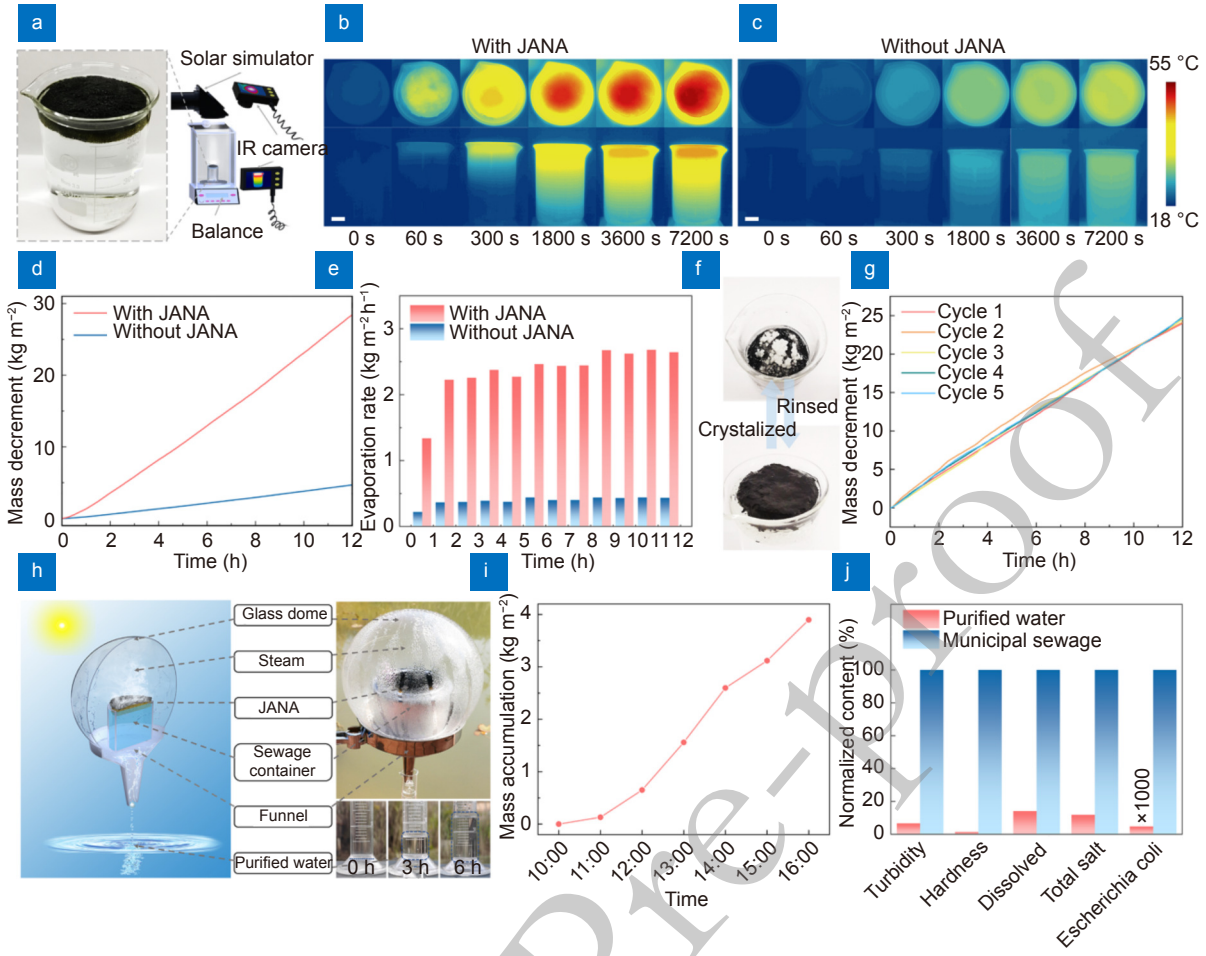

Fig. 3 | Performances of steam generation using JANA. (**a**) (left) Photograph of the tested sample where JANA floats on a beaker of water. (right) Schematic illustration of the photo-thermo-gravimetry setup to record the real-time temperature and the mass change during the steam generation process. (**b**, **c**) (up) Top- and (down) side-view IR images of the beaker during steam generation process with and without the JANA, respectively. (**d**, **e**) Mass decrements and evaporation rates of water during the steam generation process with and without JANA, respectively. (**f**) Photographs of the (up) crystallized and (down) rinsed PANA in saturated NaCl solution, respectively. (**g**) Mass decrements of saturated NaCl solution during 5 cycles of steam generation processes using a same piece of JANA. (**h**) Schematic illustration and photograph of a home-made purification setup performing realistic ISSG. Right bottom insets show the accumulation of purified water at 0 h, 3 h, and 6 h, respectively. (**i**) Correlation between purified water accumulation and time. (**j**) Normalized contents of water quality indices in purified water and municipal sewage.

evaporation of salty water can increase the concentration of solution and thus precipitate salt crystals, which would be remained on the surface of the steam generator. The salt crystals would block the solar reception of the absorber and the liquid/gas transport in the pores, and thus severely reduce the steam generation efficiency. Here, the tolerance to salt of JANA is tested under an extreme case, in which we measure the mass decrements of a beaker of saturated NaCl solution. A piece of JANA is repeatedly placed on the solution. We define a solar steam generation process with 12 h duration as a cycle. In the end of each cycle, the JANA sample is covered by NaCl crystals, as shown in Fig. 3(f). Before the beginning of the following cycle, the sample is rinsed with saturated NaCl solution. We carry out 5 cycles of solar steam generation and record the mass decrements, as shown in Fig. 3(g). Based on the mass decrements, the calculated evaporation rates vary from 2.00 to 2.07 kg m^{-2} h^{-1}, which are slightly lower to that for pure water due to salt crystal coverage. It can be seen that both the mass change profile and evaporation rate value for each cycle are almost identical, featuring a reproducible solar steam generation performance. This is attributed to the surface refreshment of JANA. NaCl crystals cannot be adsorbed by JANA via any strong physical/chemical interaction. During the rinse, the saturated NaCl solution can wet the JANA surface and flow into the pores due to the high wettability originated from the super-hydrophilicity. The

mechanical vibration of the water flow can easily wash away the salt crystals, which results in the reusability of JANA for sustainable desalination of salty water.

Furthermore, we demonstrate the availability of JANA for practical applications in water purification and collection under real solar irradiation. As shown in Fig. 3(h), we build a freshwater collector and perform purification of municipal sewage. The sewage is kept in a container with a piece of JANA sample floating on the water-air interface. The container is then placed on a funnel and covered with a transparent glass dome. Illuminated by outdoor sun light, interfacial photothermal steam generation occurs and produces plentiful purified dewdrops on the inner wall of the glass dome. With continued evaporation, dewdrops converge into streams and flow down to the funnel. The purified water is finally collected in a grad cylinder. Right bottom insets of Fig. 3(h) show the photographs of the purified water accumulations with 0 h, 3 h, and 6 h ISSG durations. The experiment is conducted from 10:00 AM to 16:00 PM with an average outdoor temperature about 20 °C. The photographs at different moments during the purification process are captured and shown in Fig. S5 of SI. Figure 3(i) gives the mass accumulation of the purified water normalized to the case that 1 m^2 JANA is used. The total collected freshwater in 6 h is 3.9 kg. The compositive water evaporation and collection rate is 0.65 kg m^{-2} h^{-1}. This value is lower than the single evaporation rate acquired in laboratory. The decrement is caused by multiple influences, including i) the solar irradiation is not constant affected by the solar altitude and atmospheric transmittance. ii) Outdoor temperature keeps fluctuating. iii) The evaporation rate is suppressed because the partial pressure of steam in the dome (a quasi-closed system) approaches to the saturated vapor pressure, which is much higher than that in laboratory. iv) The collected freshwater in the open grad cylinder can re-escape to the environment by evaporating. Nevertheless, the process of freshwater production can serve as a prototype for realistic ISSG applications and there are several optimizable conditions for potentially improvements of the yield.

Comparing the photograph of the original turbid sewage, it can be clearly seen that the purified water is much cleaner and more transparent (Fig. S6 of SI), which indicates effective ISSG purification is realized by combining JANA with the collection setup. We quantitatively analyze the purification performance. As shown in Fig. 3(j), five common quality indices in the purified water and the original sewage are tested, including the contents of turbidity, hardness, dissolved solids, total salt and Escherichia coli. For all the indices, the contents dramatically decrease after steaming purification. Detailed official report about the water quality is given in Figs. S7 and S8 of SI. These results indicate that JANA can achieve high-efficiency solar steam generation and water purification functionalities.

Mechanical and fireproof properties of JANA

JANA is of special mechanical properties. It is very soft and flexible, which facilitates the sculpture or deformation of a JANA-based device. Figure 4(a–c) respectively demonstrate that JANA can be easily cut off, rolled up, and stretched long, which result from the morphology of nanofiber network. Due to its high porosity, the number of aramid nanofibers per unit volume are extremely low. From a microscopic view, cutting a bulky JANA equals to breaking the aramid nanofibers bundle which consists of a small quantity of slender nanofibers one after another. As a result, JANA turns to be soft and a low shearing pressure is competent to cut it off. Besides, rolling and stretching a bulky JANA equals to lengthening a portion of nanofibers, which will result in the variation of the closeness between the nanofibers. These two microscopic deformations are permitted by the elasticity of the nanofibers and the porous configuration. Consequently, JANA is highly flexible. We conduct a tensile test to quantitively characterize its mechanical property, as shown in Fig. 4(d). Before broken, JANA can bear maximum tension of 19.5 MPa and perform maximum elongation of 78.9%, showing sufficient elasticity and mechanical strength. Moreover, we investigate the influence of mechanical deformation to the ISSG performance. As shown in Fig. 4(e), the water mass decrements of ISSG processes using the same JANA are measured before and after 200 times stretching with 50% strain, whose profiles are highly analogous. Therefore, JANA is of good functional stability under repeated elastic deformations.

Similar to the commercial Kevlar-based materials, JANA is also of outstanding thermal stability, resulting in its refractory and fireproof features. Figure 4(f) shows photographs of a piece of JANA directly heated by the flame from an alcohol lamp at different moments within 3 min. The fire treatment process is recorded in video S2 of SI. After the fire treatment, the downside of the JANA turns black due to the deposition of amorphous carbon

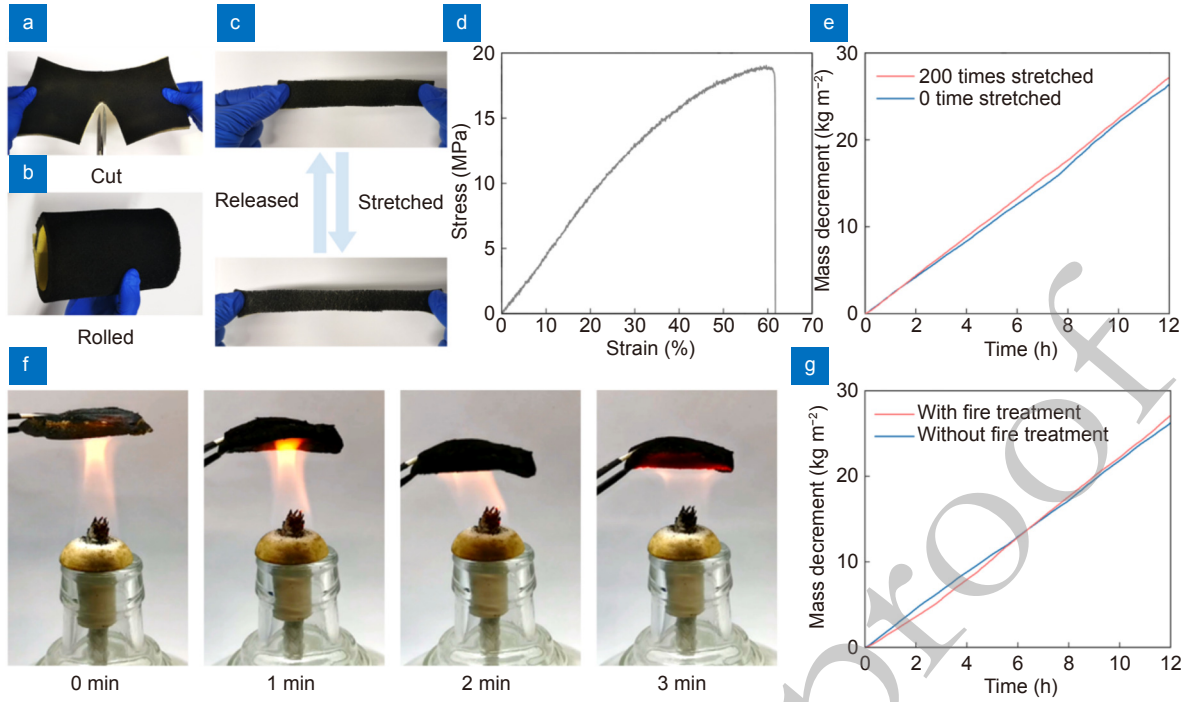

Fig. 4 | Mechanical and fireproof properties of JANA. (**a**), (**b**) and (**c**) Photographs of JANA pieces which are cut off, rolled up, and elastically stretched, respectively. (**d**) Tensile stress of JANA. (**e**) Mass decrements of steam generation processes, in which the JANA is 0 time and 200 times repeatedly stretched, respectively. (**f**) Photographs of JANA under fire treatments for 0 min, 1 min, 2 min, and 3 min. (**g**) Mass decrements of steam generation processes, in which the JANA is without and with fire treatment, respectively.

generated from the incomplete combustion of the fuel. Even though, JANA is not melted or burned, maintaining the original shape. The thermal stability can be attributed to the high melting points and chemical inertness of aramid and gold. For scenarios of fire danger, JANA can avoid damages and even retard the fire spreading, which is beneficial to safety of lives and properties. Moreover, Fig. 4(g) shows the mass decrement results of JANA-based ISSG processes before and after the fire treatment, which are nearly the same. These results imply that JANA is of excellent fireproof property and its steam generation performance is free of the fire treatment.

Conclusions

In conclusion, we demonstrate a highly scalable Janus aramid nanofiber aerogel (JANA) performing high-efficiency interfacial solar steam generation. JANA is fabricated based on a high-yield sol-gel process and its bilayer configuration consists of a solar absorber and a water transporter. The solar absorber demonstrates near-perfect, omnidirectional and broadband optical absorption, and the water transporter is porous, adiabatic and superhydrophilic. As a result, JANA performs excellent capability to heat and evaporate water during ISSG processes, by which reproducible desalination of salty water and practical purification of municipal sewage are successfully realized. In addition, JANA is flexible and fireproof, exhibiting high stability and good reusability with tolerance to mechanical deformation and fire treatment. We believe that JANA can perform higher ISSG efficiency further combined with heat recovery setups[50,51]. Besides, JANA is promising to promote the practical applications of ISSG devices, especially considering future mass industrial manufacture, convenient transportation and long-term storage.

Experimental section

Preparation of JANA

Kevlar 69 threads are swelled in dimethyl formamide forming the aramid micro fibers, which are then extracted and dispersed in a mixed solution of dimethyl sulfoxide and potassium hydroxide, which is then magnetically stirred for one week at 60 °C until a dark red viscous sol is formed. Then phosphoric acid and glutaraldehyde are added into the sol, which is then vigorously stirred for 48 h. The mixture is statically placed for 24 h forming the aramid gel, which is then successively extracted by filtration, washed using dimethyl sulfoxide, and thor-

oughly frozen at −10 °C. Afterwards, the frozen gel is taken indoors for unfreezing the gel surface. Au nanoparticle suspension is uniformly sprayed on the surface. The aramid-Au mixture is successively refrigerated at −4 °C for 24 h and freeze dried −50 °C for 8 h, forming the JANA. At last, JANA is boiled in deionized water for 30 min to remove residual dimethyl sulfoxide and qualified as a steam generator.

Characterization instruments

The microscopic morphology of the JANA is characterized by using field-emission scanning electron microscopy (FESEM, Gemini SEM 500). The porosity of JANA is measured using an AutoPore IV 9500 mercury porosimeter (Micromeritics Instrument Corporation, Norcross, GA, USA). The normal absorption spectra are tested using a PV20/30 UV-VIS-NIR spectrometer over a wavelength range of 400–2000 nm. The angular absorption spectra are measured with an ARM angle-resolved spectroscopy system (IdeaOptics Instruments). The tensile property is characterized using a SHIMADZU Universal Testing Machine AGS-X 5 kN D-Type. Evaporation experiments in Lab are carried out under a solar simulator (Newport 94043A) with the output in accordance with the standard AM 1.5G solar irradiation. A high accuracy balance (BSA124S, 1.0 mg in accuracy, Sartorius) is used for recording the mass change of water. Thermal images are taken with an Infiray (Infiray T3S) IR camera. The contact angles are characterized using a drop shape analyzer (CA100C).

References

1. Schewe J, Heinke J, Gerten D, Haddeland I, Arnell NW et al. Multimodel assessment of water scarcity under climate change. *Proc Natl Acad Sci USA* **111**, 3245–3250 (2014).
2. Elimelech M, Phillip WA. The future of seawater desalination: energy, technology, and the environment. *Science* **333**, 712–717 (2011).
3. Fritzmann C, Löwenberg J, Wintgens T, Melin T. State-of-the-art of reverse osmosis desalination. *Desalination* **216**, 1–76 (2007).
4. El-Dessouky HT, Ettouney HM, Al-Roumi Y. Multi-stage flash desalination: present and future outlook. *Chem Eng J* **73**, 173–190 (1999).
5. Wang WB, Aleid S, Shi YF, Zhang CL, Li RY et al. Integrated solar-driven PV cooling and seawater desalination with zero liquid discharge. *Joule* **5**, 1873–1887 (2021).
6. Li RY, Shi Y, Wu MC, Hong S, Wang P. Photovoltaic panel cooling by atmospheric water sorption-evaporation cycle. *Nat Sustain* **3**, 636–643 (2020).
7. Yao HZ, Zhang PP, Huang YX, Cheng HH, Li C et al. Highly efficient clean water production from contaminated air with a wide humidity range. *Adv Mater* **32**, 1905875 (2020).
8. Tao P, Ni G, Song CY, Shang W, Wu JB et al. Solar-driven interfacial evaporation. *Nat Energy* **3**, 1031–1041 (2018).
9. Wang ZX, Horseman T, Straub AP, Yip NY, Li DY et al. Pathways and challenges for efficient solar-thermal desalination. *Sci Adv* **5**, eaax0763 (2019).
10. Mi BX. Interfacial solar evaporator for brine treatment: the importance of resilience to high salinity. *Natl Sci Rev* **8**, nwab118 (2021).
11. Feng L, Huo PC, Liang YZ, Xu T. Photonic metamaterial absorbers: morphology engineering and interdisciplinary applications. *Adv Mater* **32**, 1903787 (2020).
12. Wang ZH, Liu YM, Tao P, Shen QC, Yi N et al. Bio-inspired evaporation through plasmonic film of nanoparticles at the air-water interface. *Small* **10**, 3234–3239 (2014).
13. Zhou L, Tan YL, Ji DX, Zhu B, Zhang P et al. Self-assembly of highly efficient, broadband plasmonic absorbers for solar steam generation. *Sci Adv* **2**, e1501227 (2016).
14. Zhou L, Tan YL, Wang JY, Xu WC, Yuan Y et al. 3D self-assembly of aluminium nanoparticles for plasmon-enhanced solar desalination. *Nat Photonics* **10**, 393–398 (2016).
15. Bae K, Kang GM, Cho SK, Park W, Kim K et al. Flexible thin-film black gold membranes with ultrabroadband plasmonic nanofocusing for efficient solar vapour generation. *Nat Commun* **6**, 10103 (2015).
16. Shi Y, Ilic O, Atwater HA, Greer JR. All-day fresh water harvesting by microstructured hydrogel membranes. *Nat Commun* **12**, 2797 (2021).
17. Qi DP, Liu Y, Liu YB, Liu ZY, Luo YF et al. Polymeric membranes with selective solution-diffusion for intercepting volatile organic compounds during solar-driven water remediation. *Adv Mater* **32**, 2004401 (2020).
18. Shao Y, Jiang ZP, Zhang YJ, Wang T, Zhao P et al. All-Poly(ionic liquid) Membrane-Derived porous carbon membranes: Scalable synthesis and application for photothermal conversion in seawater desalination. *ACS Nano* **12**, 11704–11710 (2018).
19. Liu FH, Zhao BY, Wu WP, Yang HY, Ning YS et al. Low cost, robust, environmentally friendly geopolymer-mesoporous carbon composites for efficient solar powered steam generation. *Adv Funct Mater* **28**, 1803266 (2018).
20. Li JL, Wang XY, Lin ZH, Xu N, Li XQ et al. Over 10 kg m^{-2} h^{-1} evaporation rate enabled by a 3D interconnected porous carbon foam. *Joule* **4**, 928–937 (2020).
21. Ren HY, Tang M, Guan BL, Wang KX, Yang JW et al. Hierarchical graphene foam for efficient omnidirectional solar-thermal energy conversion. *Adv Mater* **29**, 1702590 (2017).
22. Zhang PP, Liu F, Liao QH, Yao HZ, Geng HY et al. A microstructured graphene/poly(N-isopropylacrylamide) membrane for intelligent solar water evaporation. *Angew Chem Int Ed* **57**, 16343–16347 (2018).
23. Liang HX, Liao QH, Chen N, Liang Y, Lv GQ et al. Thermal efficiency of solar steam generation approaching 100% through capillary water transport. *Angew Chem Int Ed* **58**, 19041–19046 (2019).
24. Yang H, Sun YH, Peng MW, Cai MJ, Zhao B et al. Tailoring the salt transport flux of solar evaporators for a highly effective salt-resistant desalination with high productivity. *ACS Nano* **16**, 2511–2520 (2022).
25. Xu N, Hu XZ, Xu WC, Li XQ, Zhou L et al. Mushrooms as efficient solar steam-generation devices. *Adv Mater* **29**, 1606762

(2017).
26. Li W, Chen ZJ, Yu HP, Li J, Liu SX. Wood-derived carbon materials and light-emitting materials. *Adv Mater* **33**, 2000596 (2021).
27. Guo YH, Lu HY, Zhao F, Zhou XY, Shi W et al. Biomass-derived hybrid hydrogel evaporators for cost-effective solar water purification. *Adv Mater* **32**, 1907061 (2020).
28. Cao SS, Rathi P, Wu XH, Ghim D, Jun YS et al. Cellulose nanomaterials in interfacial evaporators for desalination: a "natural" choice. *Adv Mater* **33**, 2000922 (2021).
29. Li N, Qiao LF, He JT, Wang SX, Yu LM et al. Solar-driven interfacial evaporation and self-powered water wave detection based on an all-cellulose monolithic design. *Adv Funct Mater* **31**, 2008681 (2021).
30. Wu XH, Cao SS, Ghim D, Jiang QS, Singamaneni S et al. A thermally engineered polydopamine and bacterial nanocellulose bilayer membrane for photothermal membrane distillation with bactericidal capability. *Nano Energy* **79**, 105353 (2021).
31. Liu Y, Xiong J, Li AL, Wang RW, Wang LM et al. Plasmonic silver nanoparticle-decorated electrospun nanofiber membrane for interfacial solar vapor generation. *Text Res J* **91**, 2624–2634 (2021).
32. Guo YH, Zhou XY, Zhao F, Bae J, Rosenberger B et al. Synergistic energy nanoconfinement and water activation in hydrogels for efficient solar water desalination. *ACS Nano* **13**, 7913–7919 (2019).
33. Lu Y, Fan DQ, Wang YD, Xu HL, Lu CH et al. Surface patterning of two-dimensional nanostructure-embedded photothermal hydrogels for high-yield solar steam generation. *ACS Nano* **15**, 10366–10376 (2021).
34. Zhou XY, Guo YH, Zhao F, Shi W, Yu GH. Topology-controlled hydration of polymer network in hydrogels for solar-driven wastewater treatment. *Adv Mater* **32**, 2007012 (2020).
35. Guo YH, Zhao F, Zhou XY, Chen ZC, Yu GH. Tailoring nanoscale surface topography of hydrogel for efficient solar vapor generation. *Nano Lett* **19**, 2530–2536 (2019).
36. Zang LL, Sun LG, Zhang SC, Finnerty C, Kim A et al. Nanofibrous hydrogel-reduced graphene oxide membranes for effective solar-driven interfacial evaporation and desalination. *Chem Eng J* **422**, 129998 (2021).
37. Dong XY, Cao LT, Si Y, Ding B, Deng HB. Cellular structured CNTs@SiO_2 nanofibrous aerogels with vertically aligned vessels for salt-resistant solar desalination. *Adv Mater* **32**, 1908269 (2020).
38. Yang MQ, Tan CF, Lu WH, Zeng KY, Ho GW. Spectrum tailored defective 2D semiconductor nanosheets aerogel for full-spectrum-driven photothermal water evaporation and photochemical degradation. *Adv Funct Mater* **30**, 2004460 (2020).
39. Wu X, Robson ME, Phelps JL, Tan JS, Shao B et al. A flexible photothermal cotton-CuS nanocage-agarose aerogel towards portable solar steam generation. *Nano Energy* **56**, 708–715 (2019).
40. Zhao X, Peng LM, Tang CY, Pu JH, Zha XJ et al. All-weather-available, continuous steam generation based on the synergistic photo-thermal and electro-thermal conversion by MXene-based aerogels. *Mater Horiz* **7**, 855–865 (2020).
41. Zhao L, Bhatia B, Zhang LN, Strobach E, Leroy A et al. A passive high-temperature high-pressure solar steam generator for medical sterilization. *Joule* **4**, 2733–2745 (2020).
42. Xu Y, Guo ZZ, Wang J, Chen ZH, Yin JC et al. Harvesting solar energy by flowerlike carbon cloth nanocomposites for simultaneous generation of clean water and electricity. *ACS Appl Mater Interfaces* **13**, 27129–27139 (2021).
43. Xiong ZC, Zhu YJ, Qin DD, Chen FF, Yang RL. Flexible fire-resistant photothermal paper comprising ultralong hydroxyapatite nanowires and carbon nanotubes for solar energy-driven water purification. *Small* **14**, 1803387 (2018).
44. Zhou B, Han GJ, Zhang Z, Li ZY, Feng YZ et al. Aramid nanofiber-derived carbon aerogel film with skin-core structure for high electromagnetic interference shielding and solar-thermal conversion. *Carbon* **184**, 562–570 (2021).
45. Zhang H, Feng L, Liang YZ, Xu T. An ultra-flexible plasmonic metamaterial film for efficient omnidirectional and broadband optical absorption. *Nanoscale* **11**, 437–443 (2019).
46. Cao KQ, Siepermann CP, Yang M, Waas AM, Kotov NA et al. Reactive aramid nanostructures as high-performance polymeric building blocks for advanced composites. *Adv Funct Mater* **23**, 2072–2080 (2013).
47. Kimling J, Maier M, Okenve B, Kotaidis V, Ballot H et al. Turkevich method for gold nanoparticle synthesis revisited. *J Phys Chem B* **110**, 15700–15707 (2006).
48. Zhao YY, Ren XL, Zheng ML, Jin F, Liu J et al. Plasmon-enhanced nanosoldering of silver nanoparticles for high-conductive nanowires electrodes. *Opto-Electron Adv* **4**, 200101 (2021).
49. Zhao F, Zhou XY, Shi Y, Qian X, Alexander M et al. Highly efficient solar vapour generation via hierarchically nanostructured gels. *Nat Nanotechnol* **13**, 489–495 (2018).
50. Chiavazzo E, Morciano M, Viglino F, Fasano M, Asinari P. Passive solar high-yield seawater desalination by modular and low-cost distillation. *Nat Sustain* **1**, 763–772 (2018).
51. Alabastri A, Dongare PD, Neumann O, Metz J, Adebiyi I et al. Resonant energy transfer enhances solar thermal desalination. *Energy Environ Sci* **13**, 968–976 (2020).

Acknowledgements

This work is jointly supported by the National Natural Science Foundation of China (no. 62105142), Natural Science Foundation of Jiangsu Province (BK20220068), the Center Fundamental Research Funds for the Central Universities and Entrepreneurship and Innovation Program of Jiangsu Province (JSSCBS20210002).

Author contributions

H. Zhang and T. Xu conceived the idea and designed the project. H. Zhang, L. Feng, F. Y. Wang, and Y. Y. Zhang performed the experiments. H. Zhang, L. Feng, and M. Z. Liu analyzed the data. All authors contributed to the interpretation of results and participated in manuscript preparation. T. Xu directed the project.

Competing interests

The authors declare no competing financial interests.

Supplementary information

Supplementary information available: Chemical structure of Janus aramid nanofiber aerogel (JANA), Appearance variation of JANA with different contents of Au, Numerical simulation of the optical absorption of JANA, Wettability of aramid, Practical ISSG process using JANA, Quality inspection report of municipal sewage and purified water.
https://doi.org/10.29026/oea.2023.220061